nature geoscience

ARTICLES

https://doi.org/10.1038/s41561-019-0370-2

Ross Ice Shelf response to climate driven by the tectonic imprint on seafloor bathymetry

K. J. Tinto[1*], L. Padman[2], C. S. Siddoway[3], S. R. Springer[4], H. A. Fricker[5], I. Das[1], F. Caratori Tontini[6], D. F. Porter[1], N. P. Frearson[1], S. L. Howard[4], M. R. Siegfried[7], C. Mosbeux[5], M. K. Becker[5], C. Bertinato[1], A. Boghosian[1], N. Brady[8], B. L. Burton[9], W. Chu[10], S. I. Cordero[1], T. Dhakal[1], L. Dong[1], C. D. Gustafson[1], S. Keeshin[3], C. Locke[1], A. Lockett[3], G. O'Brien[6], J. J. Spergel[1], S. E. Starke[1], M. Tankersley[3], M. G. Wearing[1] and R. E. Bell[1]

Ocean melting has thinned Antarctica's ice shelves at an increasing rate over the past two decades, leading to loss of grounded ice. The Ross Ice Shelf is currently close to steady state but geological records indicate that it can disintegrate rapidly, which would accelerate grounded ice loss from catchments equivalent to 11.6 m of global sea level rise. Here, we use data from the ROSETTA-Ice airborne survey and ocean simulations to identify the principal threats to Ross Ice Shelf stability. We locate the tectonic boundary between East and West Antarctica from magnetic anomalies and use gravity data to generate a new high-resolution map of sub-ice-shelf bathymetry. The tectonic imprint on the bathymetry constrains sub-ice-shelf ocean circulation, protecting the ice shelf grounding line from moderate changes in global ocean heat content. In contrast, local, seasonal production of warm upper-ocean water near the ice front drives rapid ice shelf melting east of Ross Island, where thinning would lead to faster grounded ice loss from both the East and West Antarctic ice sheets. We confirm high modelled melt rates in this region using ROSETTA-Ice radar data. Our findings highlight the significance of both the tectonic framework and local ocean–atmosphere exchange processes near the ice front in determining the future of the Antarctic Ice Sheet.

The Antarctic Ice Sheet is the largest reservoir for potential global sea level rise and is the component with the highest acceleration[1,2], although its current contribution is small[2,3]. The largest recent losses of grounded ice[3] coincide with rapid, ocean-driven thinning of small ice shelves that buttress[4] the Amundsen Sea sector of the West Antarctic Ice Sheet (WAIS)[5]. The three largest Antarctic ice shelves (Ross, Filchner–Ronne and Amery) are approximately in steady state[6,7] but buttress grounded ice catchments that contain over half of the entire potential Antarctic contribution to global sea level rise (Supplementary Fig. 1), highlighting a need to understand their stability for projected future climate states.

The stability and structure of the Ross Ice Shelf (area ~480,000 km^2)[7] are controlled by the geology, glaciology and climatology of the Ross Embayment (Fig. 1). The regional geology and physiography developed from convergent tectonics within the ancient continent of Gondwana (500 million years ago (Ma)) and its protracted breakup[8,9] (190–70 Ma) (Fig. 2), which produced the thinned, subsided lithosphere under West Antarctica that is now adjacent to the thick lithosphere supporting the East Antarctic Ice Sheet (EAIS). The Ross Ice Shelf, typically a few hundred metres thick (Supplementary Fig. 2a), is formed from ice from two catchments: one from the WAIS, with 2.0 m sea level rise potential that flows as broad ice streams, and one from the EAIS, with 9.6 m sea level rise potential that flows as narrow glaciers through the Transantarctic Mountains (Supplementary Figs. 1 and 2b). Ice takes on the order of 1,000 years to flow from the grounding line to the ice front (Supplementary Fig. 2c). The ice shelf is currently stable[10] but geological evidence documents repeated collapse of the ice shelf[11] as well as large-scale retreat of the grounding line from near the continental margin at the Last Glacial Maximum[12] and more recent, substantial changes in the grounding line position and ice shelf extent during the late Holocene[13].

The East Antarctic side of the Ross Ice Shelf loses mass equally through basal melting and calving, while mass loss on the West Antarctic side is dominated by calving[6]. Satellite-derived melt rates are close to zero for much of the ice shelf, but can exceed 2 m yr^{-1} near the deep grounding lines of large EAIS glaciers and along the ice front[6,10,14,15] (Supplementary Fig. 2d). The largest observed melt rates are about 12 m yr^{-1} near Byrd Glacier's grounding line[16], and summer-only rates of about 8 m yr^{-1} have been measured close to Ross Island[17]. Melt rates are controlled by delivery of heat to the base of the ice shelf by ocean circulation that is driven by winds over the ocean north of the ice front, heat and freshwater exchanges at the ocean surface, and tides[18–20].

The ROSETTA-Ice project (Methods) included a comprehensive (10–20 km line spacing; Fig. 1b) airborne survey of the Ross Ice Shelf conducted during 2015–2017. The survey was designed to increase the resolution of seafloor bathymetry for ocean and ice sheet models and to develop new insights into the evolution of ice flow and tectonic development in the Ross Embayment. We used the IcePod instrument suite mounted on a New York Air National Guard LC-130 aircraft (Methods and Supplementary Fig. 3) to acquire gravity, magnetic, ice-penetrating radar and laser altimetry data. Together with new ocean model simulations, these measurements

[1]Lamont-Doherty Earth Observatory, Columbia University, Palisades, NY, USA. [2]Earth & Space Research, Corvallis, OR, USA. [3]Colorado College, Colorado Springs, CO, USA. [4]Earth & Space Research, Seattle, WA, USA. [5]Scripps Institution of Oceanography, University of California, San Diego, La Jolla, CA, USA. [6]GNS Science, Lower Hutt, New Zealand. [7]Colorado School of Mines, Golden, CO, USA. [8]Dynamic Gravity Systems, Broomfield, CO, USA. [9]U. S. Geological Survey, Denver, CO, USA. [10]Stanford University, Stanford, CA, USA. *e-mail: tinto@ldeo.columbia.edu

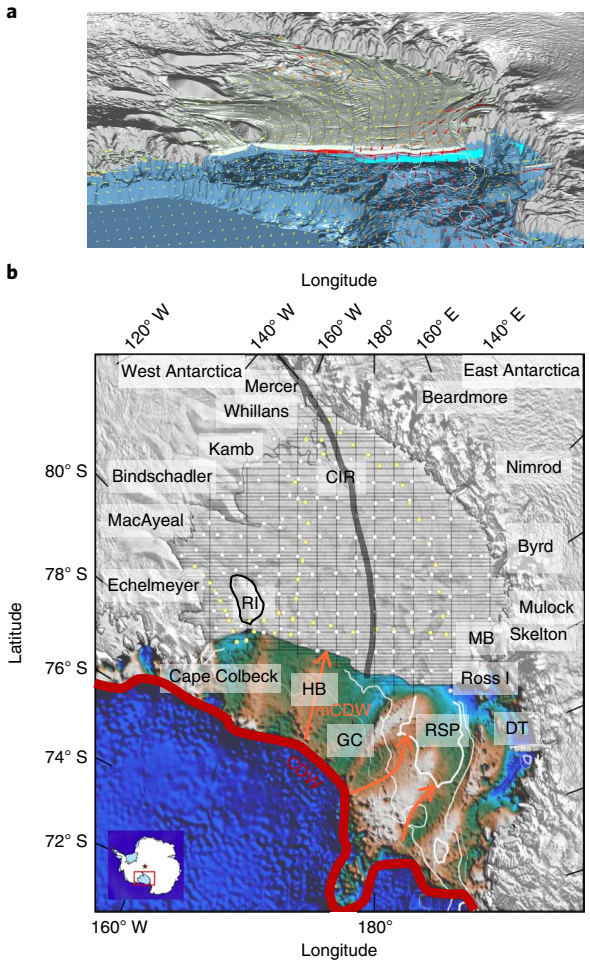

Fig. 1 | The Ross Ice Shelf within the Ross Embayment. The bathymetry (colour) is from the Bedmap2 compilation[36]. **a**, A perspective view, looking southward. The surface features (greyscale) are from Bedmap2. The arrows depict wind velocity (yellow, low; red, high). Oceanographic profile along the ice front: mCDW (red); HSSW (aqua). **b**, A map view with ROSETTA-Ice 2015–2016 survey lines in black, and 2017 lines in grey. The surface features (greyscale) are from the Moderate Resolution Imaging Spectroradiometer Mosaic of Antarctic. The thick grey line marks the boundary between ice that originated in the WAIS versus EAIS. The labels show key glaciers, ice streams and geographic places: CIR, Crary Ice Rise; RI, Roosevelt Island; HB, Hayes Bank; GC, Glomar Challenger Basin; Ross I, Ross Island; MB, Minna Bluff; DT, Drygalski Trough. The white circles mark RIGGS survey points[37], and the yellow circles mark International Geophysical Year (IGY) survey points[38]. The location of the Ross Sea Polynya (RSP) is shown as white contours of number of days of open water without sea ice; 70 (thin), 80 (medium), 90 (thick).

reveal the interconnected systems that control the stability of the Ross Ice Shelf on timescales ranging from months to millennia.

Geological structure controls sub-ice-shelf bathymetry

Magnetic anomalies from the ROSETTA-Ice surveys show an abrupt transition in character across a boundary oriented approximately north–south through the centre of the embayment (Fig. 3a). High-amplitude anomalies dominate the West Antarctic side and low-amplitude anomalies dominate the East Antarctic side. The West Antarctic crust comprises immature sedimentary rocks, magmatic arc materials and extended, thinned continental blocks[21]. High magnetic anomalies could be due to arc magmatism during convergence of Gondwana, or the exposure of highly magnetized metamorphic rocks along faults during extension[22]. The East Antarctic crust comprises ancient cratonic and orogenic material with highly variable magnetic signatures, including a low-susceptibility unit identified within the Transantarctic Mountains[23] with characteristics very similar to the East Antarctic side of the Ross Ice Shelf. We interpret the sharp boundary in magnetic character beneath the middle of the ice shelf, rather than the prominent Transantarctic Mountains front[8], to mark the position of the boundary between the East and West Antarctic crust. No obvious boundary exists in the free air gravity anomaly map (Fig. 3b), but the difference in character of the two sides is revealed in the gravity-derived density model (Fig. 3c). Density was modelled by inverting the gravity anomaly at sites where water depth is known from Ross Ice Shelf Geophysical and Glaciological Survey (RIGGS) measurements (Methods) to show the relative variation in density of a column of rock of constant thickness across the region (Fig. 3c). The denser East Antarctic side reflects thinner crust and a greater contribution from dense mantle material compared to the West Antarctic side. To attain the greater seabed depths observed on the East Antarctic side, the initially thick East Antarctic crust must have undergone a greater amount of extension than the West Antarctic crust. Different extensional histories of the two sides probably correspond to different underlying mantle properties. We interpret the boundary identified in the middle of the Ross Ice Shelf, and extending to the continental margin, as the major tectonic boundary between East and West Antarctica (Fig. 2b).

The tectonic boundary has an imprint in the bathymetry under the ice shelf, which is revealed in the new bathymetry map we developed through inversion of the ROSETTA-Ice gravity anomaly field, using the density distribution from the RIGGS-constrained model described above (Fig. 4a, Supplementary Fig. 4 and Methods). Sub-ice-shelf bathymetry is typically deeper on the East Antarctic side (670 m mean) and shallower on the West Antarctic side (560 m mean). The large-scale asymmetry in bathymetry coincides with the tectonic boundary (Fig. 2b), indicating that the asymmetry is a long-term feature that has persisted throughout multiple glacial cycles. Our new bathymetry model resolves smaller-scale features that were absent in prior grids, especially close to the grounding line where the new bathymetry is deeper near the Kamb Ice Stream and along the EAIS grounding line south of Byrd Glacier (Supplementary Fig. 4 and Methods).

Bathymetry constrains ocean circulation and basal melting

We ran an ocean circulation model (Methods), incorporating the new bathymetry and an updated ice draft. The large-scale patterns of modelled mean circulation, water mass distributions and melt rate (Fig. 4b and Supplementary Figs. 5 and 6) are similar to previous results[19,20] although we now better represent flows into the grounding zones of major East Antarctic outlet glaciers. We used simulated dyes to track the flow and modification of water masses from the deep ocean north of the continental margin to the ice shelf grounding line (Supplementary Videos 1–3). The principal water masses found along the ice front (Supplementary Fig. 7) are Antarctic Surface Water (AASW), modified Circumpolar Deep Water (mCDW), Ice Shelf Water (ISW) and High-Salinity Shelf Water (HSSW)[24]. The distributions of these water masses vary seasonally (Supplementary Fig. 5), as reported previously[20,25]. The simulation identifies the relative importance to ice shelf melting of CDW, which is part of the global thermohaline circulation, and HSSW, which is locally formed in polynyas.

The dominant inflow beneath the ice shelf, by volume, is HSSW that flows under the ice front near Ross Island and moves southward along the base of the Transantarctic Mountains. Although HSSW is at the surface freezing temperature (about −1.9 °C), it is responsible for high melting rates at the deep grounding lines of

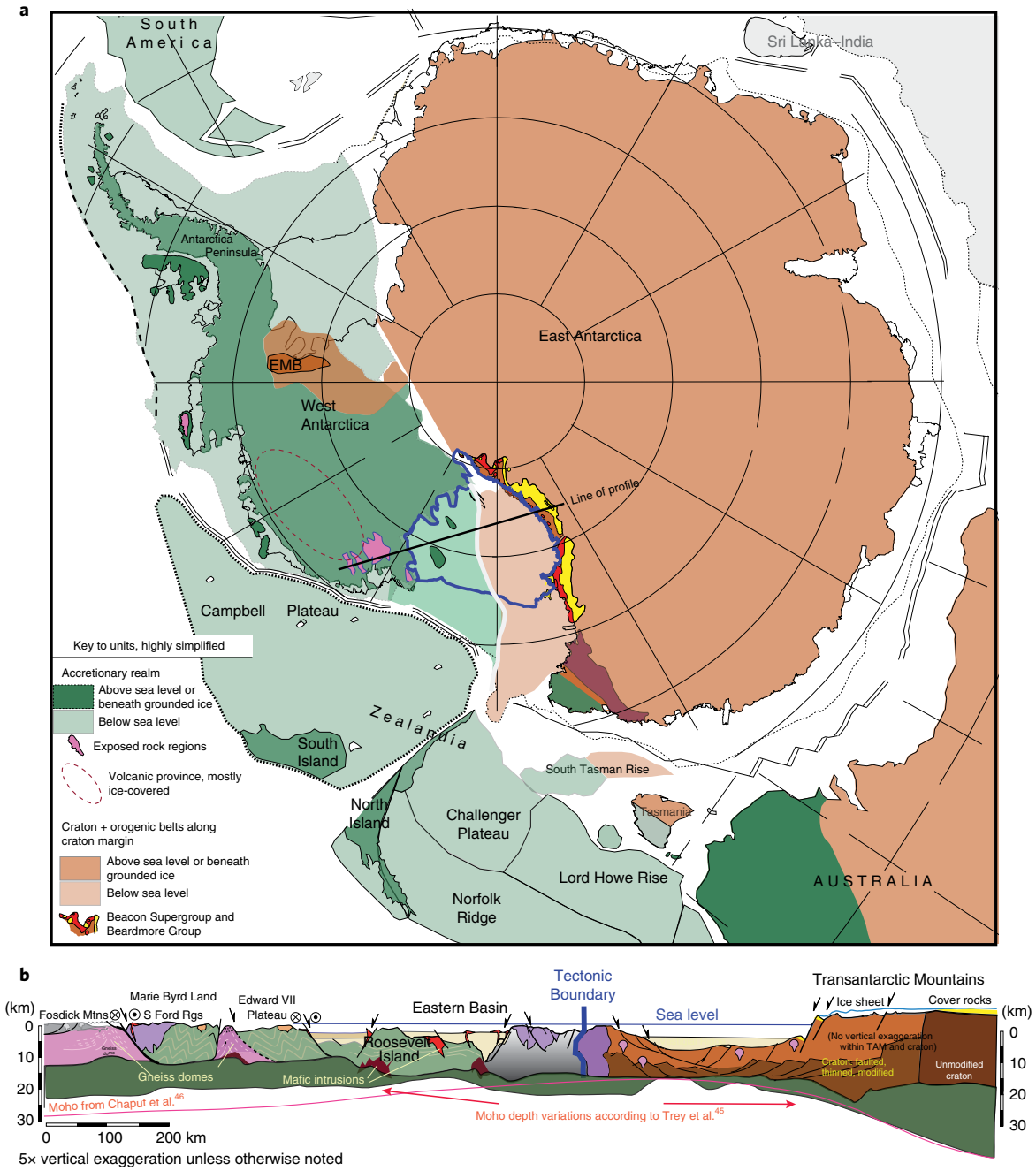

Fig. 2 | Ross Ice Shelf tectonic setting. a, A simplified tectonic map showing the position of the newly mapped tectonic boundary beneath the Ross Ice Shelf (Fig. 3), within a generalized tectonic reconstruction of the Mesozoic convergent margin of the Gondwana supercontinent. The West Antarctic accretionary province (in green shades) consists of immature sedimentary rocks, magmatic arc materials and continental blocks[21,8]. East Antarctica (brown shades) consists of ancient cratonic and orogenic crust, with overlying platform strata and dolerite in some areas[23,39,40]. Panel **a** adapted from ref. [9], Elsevier. The subglacial extent of the Ellsworth Mountains block (EMB) is from Jordan et al.[41]. **b**, A geological–tectonic cross-section across the Ross Ice Shelf region. This interpretation incorporates information from known geological relationships in rock exposures and interpretations of geophysical datasets for West Antarctica[21,22,42,43] and East Antarctica[23,40]. Low-lying lithosphere beneath the WAIS consists of comparatively young materials that have been modified by extreme crustal thinning[42,44] and displaced/rotated by rifting and wrench deformation[22,42]. Older, thick lithosphere supports the high-elevation EAIS. The East Antarctic orogenic crust that underlies a portion of the Ross Ice Shelf and Ross Sea has been affected by divergent tectonics, most notably by relative motion between continents and crustal blocks in the Weddell sector beginning at circa 200 Ma[9] and extension to transtension in the Ross sector[21,43] that preceded and accompanied separation between Australia–Zealandia and Antarctica[21]. Two contrasting models are shown for the base of the crust (Mohorovičić (Moho) discontinuity)[45,46]. Both models show thin crust but they differ in respect to the location of the shallowest Moho. S Ford Rgs, South Ford Ranges; TAM, Transantarctic Mountains.

major EAIS glaciers including Byrd[16] (Supplementary Fig. 2d) due to the pressure suppression of the freezing temperature (Methods and Supplementary Fig. 7). We find that the mixture of HSSW and ISW does not cross the tectonic boundary due to dynamic constraints imposed by the thinner water column on the West Antarctic side (Fig. 5b). Instead, it continues northward to exit the ice shelf

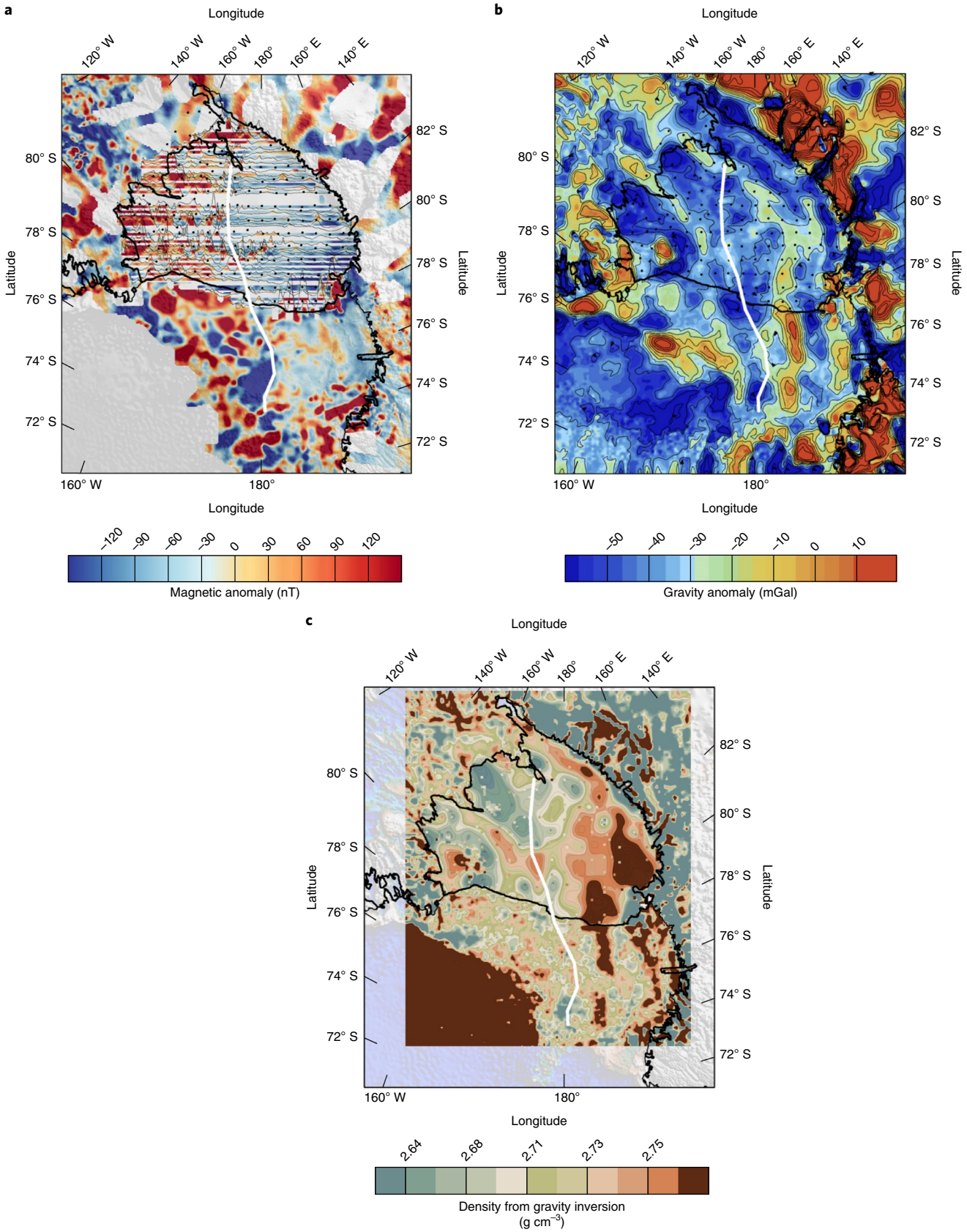

Fig. 3 | ROSETTA-Ice survey potential field results. a, The magnetic anomaly from ROSETTA-Ice within the context of the ADMAP compilation[47] for the surrounding area; the ROSETTA-Ice (2015) magnetic anomaly is represented both in colour and profile amplitudes (black lines). **b**, The free air gravity anomaly from ROSETTA-Ice (2015–2016), within the context of AntGG[48] and Ross Sea[49] gravity grids. **c**, The relative variation in density modelled from inversion of the gravity anomaly from ROSETTA-Ice and other sources where water depth is known (Methods). The white line shows the location of the boundary between the West and East Antarctic lithosphere.

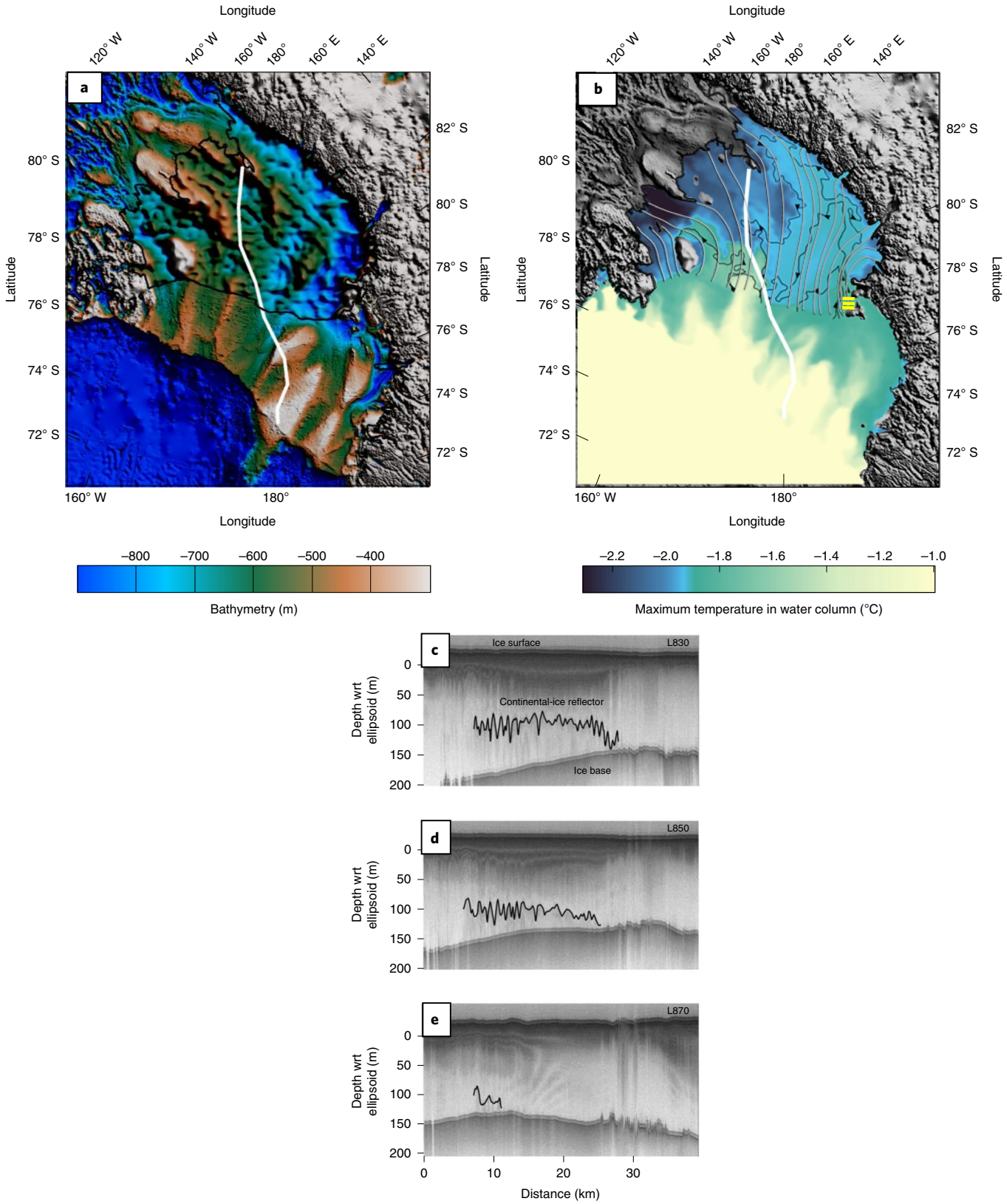

Fig. 4 | Ross Ice Shelf bathymetry, ocean temperatures and basal melt. a, Modelled bathymetry under the Ross Ice Shelf from inversion of ROSETTA-Ice gravity anomalies merged with Bedmap2 bed topography in surrounding regions. **b**, Modelled, annual averaged ocean temperature maximum in the Ross Sea. The grey lines are ice flowlines based on modern velocities (see Supplementary Fig. 2). The black lines with arrows indicate barotropic streamlines (Methods). The white line shows the location of the boundary between the West and East Antarctic lithosphere. **c**–**e**, Radargrams from the Shallow Ice Radar across ice from Mulock Glacier (location shown as yellow lines in **b**) showing progressive removal of the basal ice layer over a span of 40 km. The flow direction is from **c** to **d** to **e** (see also Supplementary Fig. 8).

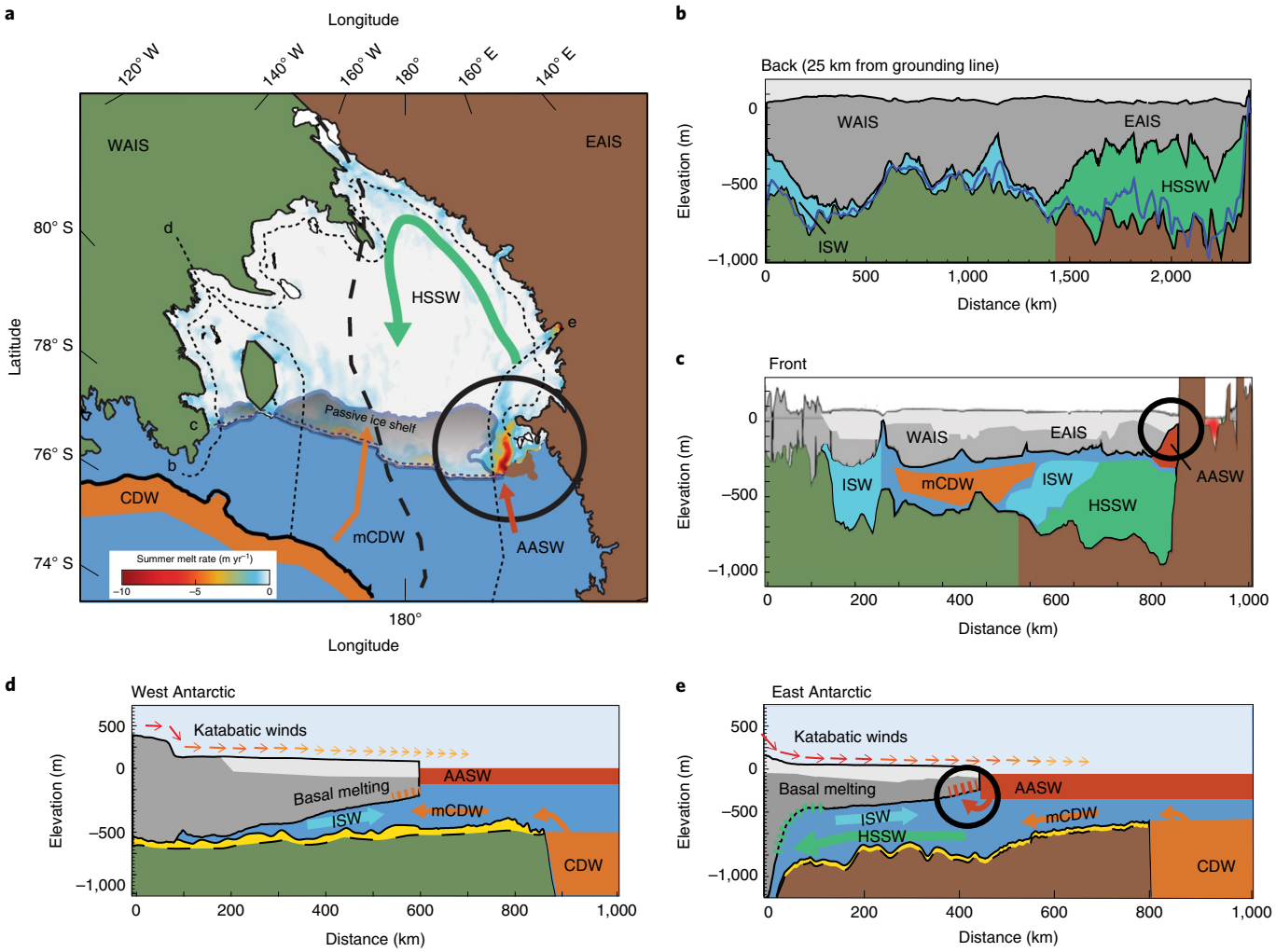

Fig. 5 | A schematic of processes controlling the Ross Ice Shelf. a, A map where fine dashed lines indicate the locations of the profiles in **b**–**e**. **b**, Back profile. **c**, Front profile. **d**, WAIS-side profile. **e**, EAIS-side profile. The black circle shows melting of a key area of vulnerability at the ice shelf front. The shaded area of the ice shelf front is the passive ice shelf of Fürst et al.[31]. The colours on the ice shelf in **a** represent summer melt rates from the model presented here. Winter processes are illustrated in Supplementary Fig. 5. The dashed line is the tectonic boundary. The water masses are labelled in colour, with arrows representing circulation. The dark green and brown blocks represent the uppermost part of the West Antarctic crust and East Antarctic crust, respectively. The grey block shows ice thickness; light grey represents ice formed as snowfall on the ice shelf. The blue line in **b** represents the previous Bedmap2 bathymetry; the ROSETTA-Ice bathymetry defines the top of the green/brown blocks. Yellow in **d** and **e** schematically represents sedimentary deposits.

cavity in the vicinity of Glomar Challenger Trough (Methods, Fig. 4b, Supplementary Fig. 5 and Supplementary Video 1).

A subsurface layer of mCDW is steered by Hayes Bank southward across the continental shelf to the ice front[26,27] (Fig. 5c and Supplementary Fig. 5). Our simulation shows some mCDW circulation and basal melting under the ice shelf to the west of Roosevelt Island (Figs. 4b and 5d, Supplementary Video 2 and Supplementary Fig. 5e,f). However, the penetration of the mCDW is limited to a region within about 100 km of the ice shelf front. Further south, the WAIS side of the ice shelf is isolated from this source of oceanic heat and is dominated by a sluggish pool of very cold ISW (Methods, Fig. 5b and Supplementary Figs. 5 and 6), leading to negligible melt rates there (Supplementary Fig. 5e,f).

Relatively high modelled melt rates along the ice front are consistent with satellite-based estimates[14,15]. Annual-averaged rates are dominated by rapid melting in summer (Supplementary Fig. 5f) due to warmer inflows of mCDW along Hayes Bank and the presence of seasonally warmed AASW along the ice front. The highest seasonal melt rates are found on the East Antarctic side close to Ross Island (Supplementary Fig. 5f) where thinner ice at the front permits flows of AASW under the ice shelf[17,20,28] (Fig. 5e, Supplementary Fig. 5f and Supplementary Video 3).

Radar observations of basal melt near the ice shelf front

We use cross-sections of ice shelf vertical structure from the ROSETTA-Ice Shallow Ice Radar to identify thinning along East Antarctic ice flowlines, providing a direct measurement of changing ice thickness, interpreted as basal melt, averaged over timescales of decades to centuries (Methods). The radar identifies the internal boundary between a lower layer of ice formed on the continent, and younger ice formed from snowfall onto the ice shelf (Fig. 4c–e and Supplementary Fig. 8). The continental-ice layer along the Mulock Glacier flowline thins by more than 75 m over a distance of 40 km (Fig. 4c–e) during ~82 years (Supplementary Fig. 4c), reaching zero thickness about 50 km south of the ice front. On the basis of these observations, the steady thinning rate for this layer over the last ~80 years is 0.9 m yr^{-1}. Thickness change is a combination of basal mass balance and ice divergence. Strain rates calculated from

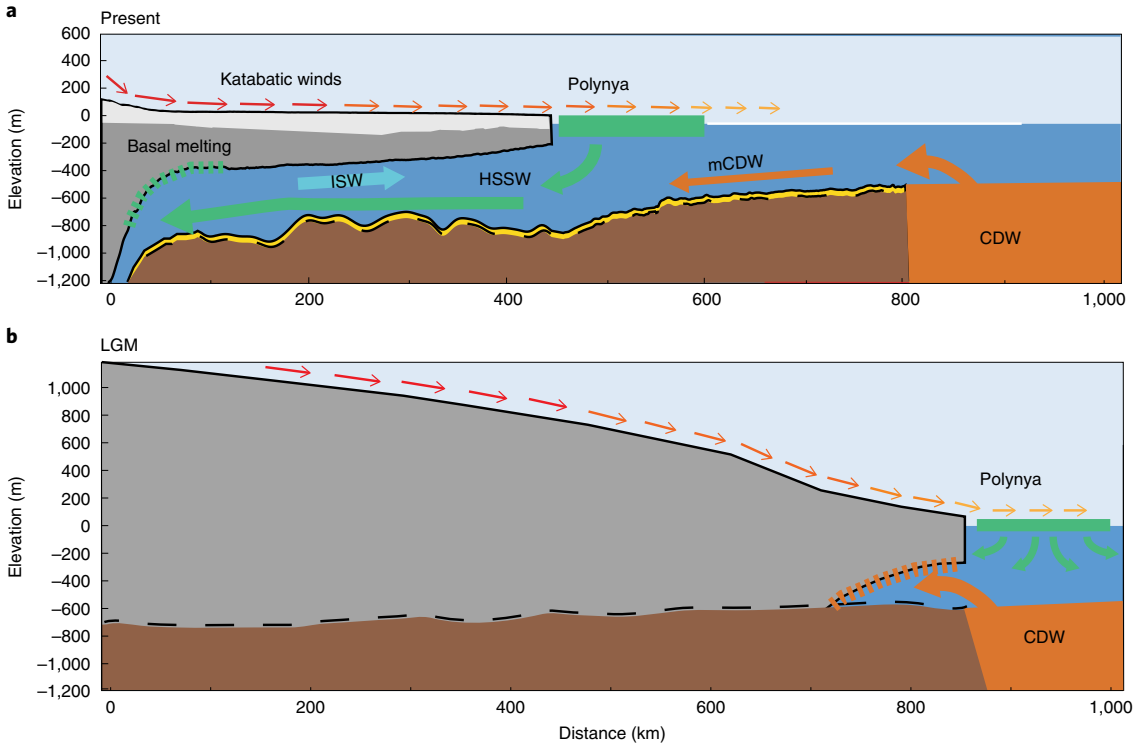

Fig. 6 | A schematic comparing wintertime interactions between Ross Ice Shelf katabatic winds, local (HSSW) and global (CDW) major water masses during modern and glacial times. a, Under present-day conditions, convection to the seabed creates HSSW, which protects the ice shelf from global ocean warmth, as mCDW does not penetrate beneath the ice shelf on the EAIS side of the tectonic boundary. **b**, During the Last Glacial Maximum (LGM), when the ice front was near the continental shelf edge, relatively unmodified CDW could enter the ice shelf cavity. Cold water formed in the polynya mixed with the CDW layer in the upper ocean.

a satellite-derived ice velocity field[15] suggest that compressive flow in this region causes 0.33 m yr^{-1} thickening of this layer. Applying this strain correction to the observed thinning rate gives a basal melt rate of 1.23 m yr^{-1}, matching the 1.2 ± 0.2 m yr^{-1} basal melt rate derived from satellite altimetry[15] (Methods). The close match between our method and the satellite altimetry result suggests that the processes currently melting the EAIS ice near Ross Island have persisted throughout the last century.

Future vulnerability and past ice sheet processes

Our results indicate that the tectonically controlled asymmetry in the bathymetry will prevent basal melt rates at the grounding line from changing substantially for future moderate changes in climate, in agreement with Dinniman et al.[19]. In this case, melt rates at the deep grounding lines of EAIS glaciers will remain high, but stable, since they are controlled by HSSW whose temperature remains constant (about −1.9 °C) and whose circulation is strongly controlled by bathymetry. Melt rates near WAIS grounding lines will remain low since the large-scale circulation accumulates very cold meltwater in this region, and the thinness of the ocean cavity on the West Antarctic side of the tectonic boundary provides a strong dynamic barrier to incursions of global ocean heat from mCDW inflows.

In the near term, the primary sensitivity of the mass balance of the Ross Ice Shelf will be to variations in local climate that change melt rates near the ice front[17,20,28]. Changes in frontal melt may be driven by changes in the amount of mCDW flowing south across the continental shelf along Hayes Bank (Supplementary Fig. 5), and by variable summer production of AASW. The mCDW heat flux depends on large-scale climate processes that determine the rate at which CDW (with temperature greater than 0 °C) is forced onto the continental shelf, and subsequent heat loss from the mCDW by mixing and upper ocean convection in winter. The production rate and properties of AASW are strongly influenced by local sea ice conditions, freshwater influx from the Amundsen Sea[29] influencing heat content and upper ocean stability, and the net atmospheric heat flux[30].

The effect of changing ice shelf melt rates on ice sheet stability depends on the local contribution of the ice to net buttressing of the grounded ice flow. Most of the ice front is 'passive shelf ice'[31] (Fig. 5). Any ice loss from this region will have only a small effect on the acceleration of grounded ice flow. In contrast, ice shelf thinning or retreat near Ross Island will reduce buttressing of nearby EAIS glaciers as well as the more distant WAIS ice streams[32]. We propose that the grounded ice catchments around the Ross Embayment are most vulnerable to ice shelf loss near the ice shelf front around Ross Island and Minna Bluff, specifically due to increases in the duration and intensity of summer production of warm AASW and its subsequent flow under the ice shelf[17,19,20,28].

On longer timescales, the role of local climate variations in destabilizing the Ross Ice Shelf will have depended on the position of the ice front. During the Last Glacial Maximum the ice sheet grounding line was near the edge of the continental shelf[12]. In this configuration, locally formed water masses are likely to have played a lesser role as the globally controlled, relatively warm CDW could flow into the sub-ice cavity, generating high melt rates at the grounding line similar to those observed in the present-day Amundsen Sea[33] (Fig. 6). During the subsequent retreat of the ice sheet, the ability of wind-forced ice-front polynyas to produce colder HSSW would have been established. As the HSSW filled the ice shelf cavity, the Ross Ice Shelf system would have shifted to a locally controlled, cold, sub-ice cavity[18]. This switch from global to local controls should be preserved in the geological record of former ice shelf extent, including existing sediment cores[11].

As the grounded ice retreated after the Last Glacial Maximum, the East and West Antarctic ice sheets would have responded differently to the bathymetry on either side of the tectonic boundary. In the Ross Sea north of the modern ice shelf, the bathymetric expression of the boundary is buried by extensive Cenozoic sediments, so will not have had direct influence on the retreat of the grounding line across this region. Instead, the bathymetry of this region has been sculpted by glacial deposition and erosion[12]. Beneath the present-day Ross Ice Shelf, the bathymetry clearly reflects the tectonic boundary. The deep bathymetric troughs connected to Nimrod and Byrd glaciers would have aided the rapid grounding line retreat inferred on the East Antarctic side[34]. The shallow West Antarctic side, with pinning points such as the present-day Roosevelt Island, Steershead Ice Rise and Crary Ice Rise, will have experienced slower ice sheet retreat.

The contrasting crustal properties across the tectonic boundary also introduce different basal boundary conditions, modulating the flow of the grounded EAIS and WAIS ice during prior glacial epochs. Crustal properties control the production and localization of geothermal heat flux as well as influencing the lithosphere's isostatic response to ice loading and unloading. The response to changing ice load plays a key role in the WAIS grounding line history around Crary Ice Rise[35], which lies on the boundary between the East and West Antarctic crust. The ice sheets will have produced different isostatic responses as they retreated across the different material on either side of this tectonic boundary.

Our survey results have shown that the bathymetry and basal boundary conditions under the Ross Ice Shelf have a tectonic origin, indicating that the contrasting conditions under the WAIS and EAIS sectors have endured through the entire glacial history of the Ross Embayment. Under the present-day Ross Ice Shelf, the newly identified tectonic boundary controls the shape of the sub-ice-shelf cavity, enabling circulation that insulates the grounding line from the influence of global ocean heat. We have identified that the greatest vulnerability of both the East and West Antarctic ice sheets in the Ross Sea sector is to local, seasonal, upper-ocean warming and deepening of the surface layer at a key region of the ice front, near Ross Island. This finding highlights the need to incorporate the ice shelf response to local climate processes in large-scale predictions of ice sheet behaviour in the broader tectonic framework.

Online content

Any methods, additional references, Nature Research reporting summaries, source data, statements of code and data availability and associated accession codes are available at https://doi.org/10.1038/s41561-019-0370-2.

Received: 8 November 2018; Accepted: 8 April 2019;
Published online: 27 May 2019

References

1. Nerem, R. et al. Climate-change–driven accelerated sea-level rise detected in the altimeter era. *Proc. Natl Acad. Sci. USA* **115**, 2022–2025 (2018).
2. Shepherd, A. et al. Mass balance of the Antarctic ice sheet from 1992 to 2017. *Nature* **558**, 219–222 (2018).
3. Gardner, A. S. et al. Increased West Antarctic and unchanged East Antarctic ice discharge over the last 7 years. *Cryosphere* **12**, 521–547 (2018).
4. Dupont, T. K. & Alley, R. B. Assessment of the importance of ice-shelf buttressing to ice-sheet flow. *Geophys. Res. Lett.* **32**, L04503 (2005).
5. Pritchard, H. D. et al. Antarctic ice-sheet loss driven by basal melting of ice shelves. *Nature* **484**, 502 (2012).
6. Rignot, E., Jacobs, S., Mouginot, J. & Scheuchl, B. Ice-shelf melting around Antarctica. *Science* **341**, 266–270 (2013).
7. Depoorter, M. A. et al. Calving fluxes and basal melt rates of Antarctic ice shelves. *Nature* **502**, 89–92 (2013).
8. Dalziel, I. & Lawver, L. in *The West Antarctic Ice Sheet: Behavior and Environment* (eds Alley, R. B. & Bindschadler, R. A.) 29–44 (American Geophysical Union, 2001).
9. Veevers, J. J. Reconstructions before rifting and drifting reveal the geological connections between Antarctica and its conjugates in Gondwanaland. *Earth Sci. Rev.* **111**, 249–318 (2012).
10. Paolo, F. S., Fricker, H. A. & Padman, L. Volume loss from Antarctic ice shelves is accelerating. *Science* **348**, 327–331 (2015).
11. Naish, T. et al. Obliquity-paced Pliocene West Antarctic ice sheet oscillations. *Nature* **458**, 322–328 (2009).
12. Anderson, J. B. et al. Ross Sea paleo-ice sheet drainage and deglacial history during and since the LGM. *Quat. Sci. Rev.* **100**, 31–54 (2014).
13. Yokoyama, Y. et al. Widespread collapse of the Ross Ice Shelf during the late Holocene. *Proc. Natl Acad. Sci. USA* **113**, 2354–2359 (2016).
14. Horgan, H. J., Walker, R. T., Anandakrishnan, S. & Alley, R. B. Surface elevation changes at the front of the Ross Ice Shelf: implications for basal melting. *J. Geophys. Res.* **116**, C02005 (2011).
15. Moholdt, G., Padman, L. & Fricker, H. A. Basal mass budget of Ross and Filchner–Ronne ice shelves, Antarctica, derived from Lagrangian analysis of ICESat altimetry. *J. Geophys. Res. Earth Surf.* **119**, 2361–2380 (2014).
16. Kenneally, J. P. & Hughes, T. J. Basal melting along the floating part of Byrd glacier. *Antarct. Sci.* **16**, 355–358 (2004).
17. Stewart, C. L., Christoffersen, P., Nicholls, K. W., Williams, M. J. M., Dowdeswell, J. A. Basal melting of Ross Ice Shelf from solar heat absorption in an ice-front polynya. *Nat. Geosci.* https://doi.org/10.1038/s41561-019-0356-0 (2019).
18. MacAyeal, D. R. Thermohaline circulation below the Ross Ice Shelf: a consequence of tidally induced vertical mixing and basal melting. *J. Geophys. Res.* **89**, 597–606 (1984).
19. Dinniman, M. S., Klinck, J. M., Hofmann, E. E. & Smith, W. O.Jr. *Effects of projected changes in wind, atmospheric temperature, and freshwater inflow on the Ross Sea. J. Clim.* **31**, 1619–1635 (2018).
20. Assmann, K., Hellmer, H. & Beckmann, A. Seasonal variation in circulation and water mass distribution on the Ross Sea continental shelf. *Antarct. Sci.* **15**, 3–11 (2003).
21. Siddoway, C. S. in *Antarctica: A Keystone in a Changing World* (eds Cooper, A. K. et al.) Ch. 9, 91–114 (National Academy of Sciences, 2008).
22. Luyendyk, B. P., Wilson, D. S. & Siddoway, C. S. The eastern margin of the Ross Sea rift in western Marie Byrd Land: crustal structure and tectonic development. *Geochem. Geophys. Geosyst.* **4**, 1090 (2003).
23. Goodge, J. W. & Finn, C. A. Glimpses of East Antarctica: aeromagnetic and satellite magnetic view from the central Transantarctic Mountains of East Aantarctica. *J. Geophys. Res.* **115**, B09103 (2010).
24. Orsi, A. H. & Wiederwohl, C. L. A recount of Ross Sea waters. *Deep-Sea Res. II* **56**, 778–795 (2009).
25. Jendersie, S., Williams, M. J., Langhorne, P. J. & Robertson, R. The density-driven winter intensification of the Ross Sea circulation. *J. Geophys. Res. Oceans* **123**, 7702– 7724.
26. Smith, W. O. Jr, Sedwick, P. N., Arrigo, K. R., Ainley, D. G. & Orsi, A. H. The Ross Sea in a sea of change. *Oceanography* **25**, 90–103 (2012).
27. Smethie, W. M. Jr & Jacobs, S. S. Circulation and melting under the Ross Ice Shelf: estimates from evolving CFC, salinity and temperature fields in the Ross Sea. *Deep-Sea Res. I* **52**, 959–978 (2005).
28. Stern, A. A., Dinniman, M. S., Zagorodnov, V., Tyler, S. W. & Holland, D. M. Intrusion of warm surface water beneath the McMurdo ice shelf, Antarctica. *J. Geophys. Res. Oceans* **118**, 7036–7048 (2013).
29. Jacobs, S. S. & Giulivi, C. F. Large multidecadal salinity trends near the Pacific–Antarctic continental margin. *J. Clim.* **23**, 4508–4524 (2010).
30. Schneider, D. P. & Reusch, D. B. Antarctic and Southern Ocean surface temperatures in CMIP5 models in the context of the surface energy budget. *J. Clim.* **29**, 1689–1716 (2016).
31. Fürst, J. J. et al. The safety band of Antarctic ice shelves. *Nat. Clim. Change* **6**, 479–482 (2016).
32. Reese, R., Gudmundsson, G. H., Levermann, A. & Winkelmann, R. The far reach of ice-shelf thinning in Antarctica. *Nat. Clim. Change*. **8**, 53–57 (2018).
33. Dutrieux, P. et al. Strong sensitivity of Pine Island ice-shelf melting to climatic variability. *Science* **343**, 174–178 (2014).
34. Spector, P. et al. Rapid early-Holocene deglaciation in the Ross Sea, Antarctica. *Geophys. Res. Lett.* **44**, 7817–7825 (2017).
35. Kingslake, J. et al. Extensive retreat and re-advance of the West Antarctic Ice Sheet during the Holocene. *Nature* **558**, 430–434 (2018).
36. Fretwell, P. et al. Bedmap2: Improved ice bed, surface and thickness datasets for Antarctica. *Cryosphere* **7**, 375–393 (2013).
37. Bentley, C. R. & Hayes, D. E. (eds) *The Ross Ice Shelf: Glaciology and Geophysics* (American Geophysical Union, 1990).
38. Crary, A. P. *Glaciological Studies at Little America Station, Antarctica, 1957 and 1958* (American Geographical Society, 1961).
39. Cawood, P. A. Terra Australis Orogen: Rodinia breakup and development of the Pacific and Iapetus margins of Gondwana during the Neoproterozoic and Paleozoic. *Earth Sci. Rev.* **69**, 249–279 (2005).
40. Elliot, D. H. *The Geological and Tectonic Evolution of the Transantarctic Mountains: A Review* (Geological Society, 2013).

41. Jordan, T. et al. Inland extent of the Weddell Sea rift imaged by new aerogeophysical data. *Tectonophysics* **585**, 137–160 (2013).
42. McFadden, R. R., Siddoway, C. S., Teyssier, C. & Fanning, C. M. Cretaceous oblique extensional deformation and magma accumulation in the Fosdick Mountains migmatite-cored gneiss dome, West Antarctica. *Tectonics* **29**, TC4022 (2010).
43. Karner, G. D., Studinger, M. & Bell, R. E. Gravity anomalies of sedimentary basins and their mechanical implications: application to the Ross Sea basins, West Antarctica. *Earth Planet. Sci. Lett.* **235**, 577–596 (2005).
44. Siddoway, C. S., Baldwin, S., Fitzgerald, P. G., Fanning, C. M. & Luyendyk, B. P. Ross Sea mylonites and the timing of intracontinental extension within the West Antarctic rift system. *Geology* **32**, 57–60 (2004).
45. Trey, H. et al. Transect across the West Antarctic rift system in the Ross Sea, Antarctica. *Tectonophysics* **301**, 61–74 (1999).
46. Chaput, J. et al. The crustal thickness of West Antarctica. *J. Geophys. Res. Solid Earth* **119**, 378–395 (2014).
47. Golynsky, A. et al. in *Antarctica, Contributions to Global Earth Sciences* (eds Fütterer, D. K. et al.) 109–116 (Springer, 2006).
48. Scheinert, M. et al. New Antarctic gravity anomaly grid for enhanced geodetic and geophysical studies in Antarctica. *Geophys. Res. Lett.* **43**, 600–610 (2016).
49. Sandwell, D. T., Müller, R. D., Smith, W. H., Garcia, E. & Francis, R. New global marine gravity model from CryoSat-2 and Jason-1 reveals buried tectonic structure. *Science* **346**, 65–67 (2014).

Acknowledgements

We gratefully acknowledge the support of the 109th Airlift Wing of the New York Air National Guard. We thank the United States Antarctic Program and staff of McMurdo Station seasons 2014–2018 and J. DeTemple during the development of the IcePod. This work was supported by the National Science Foundation 0958658, 1443534, 1443498, 1443677, 1443497 and 1341688, NASA NNX16AJ65G, the Moore Foundation, the Old York Foundation, the New Zealand Ministry of Business Innovation and Employment contract C05X1001, and New Zealand Antarctic Research Institute (NZARI no. 2014-11) funded Aotearoa New Zealand Ross Ice Shelf Programme (F.C.T. and G.O'B.). Any use of trade, firm, or product names is for descriptive purposes only and does not imply endorsement by the United States Government.

Author contributions

K.J.T., R.E.B., L.P., C.S.S., S.R.S., H.A.F., I.D. and F.C.T. conceived the experiment and analysed the data; D.F.P. contributed to oceanography; M.R.S. and C.M. contributed to glaciology; S.L.H. contributed to developing and running the ocean model simulations; N.P.F., C.B., T.D., W.C. and L.D. developed the IcePod instrument suite and acquired the data; S.K. analysed radar data; M.T. contributed to the bathymetry model; M.K.B., A.B., N.B., B.L.B., S.I.C., C.D.G., C.L., A.L., G.O'B., J.J.S., S.E.S. and M.G.W. acquired and processed data in the field.

Competing interests

N.B. is director of operations of Dynamic Gravity Systems, provider of one of the gravity instruments used in the ROSETTA-Ice surveys. The remaining authors declare no competing interests.

Additional information

Supplementary information is available for this paper at https://doi.org/10.1038/s41561-019-0370-2.

Reprints and permissions information is available at www.nature.com/reprints.

Correspondence and requests for materials should be addressed to K.J.T.

Publisher's note: Springer Nature remains neutral with regard to jurisdictional claims in published maps and institutional affiliations.

Methods

Survey design. Ross Ocean and ice Shelf Environment, and Tectonic setting Through Aerogeophysical surveys and modeling (ROSETTA-Ice) is a multi-disciplinary investigation of the lithosphere–ocean–ice-sheet system of the Ross Ice Shelf (Fig. 1). This ice shelf was last systematically surveyed in 1973–1978 by the RIGGS programme[37], which occupied stations on a ~55 km grid (Fig. 1b) with measurements of ice thickness, water depth, snow accumulation, velocity and strain. The RIGGS programme also successfully completed the first borehole through the ice shelf into the underlying water-filled cavity at site J-9[50].

The ROSETTA-Ice survey was a comprehensive aerogeophysical grid (Fig. 1b), acquired over the Ross Ice Shelf during three field seasons (November–December 2015, 2016, 2017) using the IcePod integrated sensing system (Supplementary Fig. 3) and pallet-mounted gravity systems. IcePod's instrumentation suite includes: a Scintrex caesium magnetometer and a Billingsley fluxgate magnetometer; the Deep Ice Radar (a pulsed-chirp depth-sounding radar with 1,200 W power output with a 60 MHz bandwidth and 188 MHz centre frequency); the Shallow Ice Radar (600 MHz bandwidth, 1 ms chirp shallow-ice radar with a power output of ~1 W at a 2 GHz centre frequency); visual and infrared cameras; a Riegl VQ-580 scanning laser; Global Positioning System/inertial navigation system positioning systems; and a data acquisition system.

The gravity systems included a LaCoste and Romberg S-80 dynamic gravity meter upgraded to a ZLS Ultrasys control system, a Dynamic Gravity System (DgS) Airborne Gravity Meter and an iMar NAV-RQH-001 strapdown gravity system. The IcePod system and the gravity instruments were installed on New York Air National Guard LC-130 aircraft based at McMurdo Station on Ross Island.

The ROSETTA-Ice main survey lines were spaced at 10 km and oriented east–west, with north–south-oriented tie lines spaced at 55 km. Flight elevation was on average 750 m above ground level at a flight speed of 180 knots. The grid was oriented to overfly as many RIGGS stations as possible. The data presented here are from the 2015 and 2016 field seasons where line spacing generally varies from 10 to 20 km. The maps use the polar stereographic projection EPSG 3031 with the scale true at 71° S, origin 90° S, 0° E.

Magnetic data reduction. Magnetic anomalies (Fig. 3a) were acquired with a Scintrex Cs3 caesium sensor and a Billingsley fluxgate magnetometer. Fluxgate data were used to compensate Cs3 data for aircraft motion. Diurnal variation was measured at McMurdo Station and corrected along flight lines.

Magnetic data were cleaned and filtered to remove noise. Filtering at 10 s at an average flight speed of 180 knots (93 m s^{-1}) limits the shortest wavelengths that can be recovered from the dataset to 930 m. Given a flight elevation of 750 m and average seafloor depth of 600 m, surveys are flown roughly 1,350 m above the seafloor, so filter length allows all geologically sourced magnetic anomalies at this flight elevation to be recovered.

Gravity data reduction. Gravity anomalies (Fig. 3b) used in this analysis were acquired from the ZLS gravimeter, an iMAR inertial measurement unit and a DgS gravimeter. ZLS values were tied to the absolute base station at McMurdo using a LaCoste–Romberg D-meter ground calibration. Where ZLS data were of low quality (during changes in elevation, at the end of lines or where turbulence was experienced in flight), iMAR or DgS data were used. The iMAR system is sensitive to short-wavelength gravity anomalies, but prone to drift over longer wavelengths. The iMAR data were levelled to the local, long-wavelength level of the ZLS gravimeter. The gravity dataset from the combined instrument measurements was levelled to ensure a self-consistent anomaly, with mean crossovers of 2.9 mGal for the acquired grid. Flight line data were gridded using minimum curvature at 2 km cell size.

Density model from gravity data. The density model (Fig. 3c) was developed by inverting the combined ROSETTA-Ice gravity anomaly grid over areas with known bathymetry. Bathymetry/topography constraints came from three regions: grounded ice, where ice thickness is measured by radar sounding; in the Ross Sea north of the ice front, where water thickness is measured with ship-based acoustic surveys; and under the ice shelf at points where water depth is known from seismic shots. Ice shelf constraints were taken from the seismic surveys of the RIGGS[37] project and surface traverses travelled in the International Geophysical Year (IGY)[38]. Regions of grounded ice and floating ice were distinguished using the ice shelf grounding line from Depoorter et al.[7]. We assumed that the Ross Ice Shelf grounding line is stationary over decadal timescales[51].

We calculated a forward model of gravity from these known constraints. For grounded ice we used the 1 km cell size grid of Bedmap2[36] and for the open ocean we used the 0.5 km grid of the International Bathymetric Chart of the Southern Ocean[52]. Both grids were smoothed to 2 km to match the gravity anomaly grid. For the area under the ice shelf, bathymetry was smoothly gridded between known points. With an initial density estimate of 2.67 g cm^{-3} across the model region, and the rock layer extending to 60 km deep, we inverted the observed gravity using the Geosoft GMSys 3D software package to produce a density model. This new density model accounts for the residuals caused by large-scale variations in density, controlling the differing relationship between points of known bathymetry and the observed gravity, as well as short-wavelength features of the gravity anomaly that reflect short-wavelength variation in seafloor bathymetry. To apply the modelled density to a bathymetry model, we filtered the density model to remove length scales less than ~50 km (Fig. 3c). No Moho model was applied in this analysis. Moho models of the region[46,53,54] indicate a large-scale trend towards thinner crust on the East Antarctic side. There is no such large-scale trend apparent in the free air gravity anomaly from the ROSETTA-Ice survey region, suggesting that the gravity effects of the thinner crust are compensated by the difference in bathymetry and shallow crustal geology across the region. Our method combines the effects of deep and shallow structures into a single density at each point of the inversion, and could result in either an over- or underestimation of the density of rock on the seafloor.

Bathymetry from gravity data. Airborne gravity data have been used extensively to constrain bathymetry beneath ice shelves and floating ice tongues in Antarctica[55–59] and Greenland[60,61]. The measured gravity anomaly shows the same form as bed topography where it is known either from radar echo sounding over grounded ice or acoustic sounding from ships (Supplementary Fig. 9). The sub-ice topography along the Siple Coast is strongly incised, with up to 600 m relief and a range of ~80 mGal (Supplementary Fig. 9a) while the bathymetry of the Ross Sea is more subdued, with less than 200 m relief and a range of ~25 mGal (Supplementary Fig. 9c). The gravity signature of the Ross Ice Shelf line (Supplementary Fig. 9b) is most similar to the Siple Coast on its West Antarctic side and to the Ross Sea on its East Antarctic side. The Ross Sea profile demonstrates how the thick drape of Cenozoic sediment has subdued the gravity signal of the variations in the underlying West Antarctic-style crust. RIGGS seismic control points provide water depth constraints beneath the Ross Ice Shelf at 55 km spacing and allow large-scale variations in rock density to be accounted for. The strong contrast in density between rock (~2.67 g cm^{-3}) and seawater (1.028 g cm^{-3}) at the seafloor is well expressed because it is nearest to the sensor and greater in magnitude than the contrasts arising from geological variations (contrast typically less than 1 g cm^{-3}) at depth below the seabed. The long-wavelength variation in bathymetry is known from point measurements made across the ice shelf region, and the density model derived from these known points accounts for long-wavelength variations in the gravity field. Short-wavelength variations are attributed to the small-scale variability of seafloor depth and the observed gravity anomaly is inverted again to model the seafloor variations (Fig. 4a). Points where water depth is known from RIGGS points or where ice is identified as grounded in the Bedmap2 compilation are held fixed in the inversion.

The uncertainty of the gravity measurements is 2.9 mGal from crossovers in the survey grid (Fig. 1b). The gravity inversion provides an appropriate fit given the accuracy of the measurements, with 3.2 mGal standard deviation of residuals after inversion. The uncertainty of the bathymetry constraints is 10 m under grounded ice, 5–10 m in open water where depth data are known from ship-based acoustic surveys[62], and about 10 m under the ice shelf where it is a result of the RIGGS and IGY seismic measurements. The uncertainty of the gridded bathymetry datasets is higher where no direct measurements have been made. The interpolation of bathymetry points under the ice shelf uses a 10 km cell size, so the uncertainty in the location of early bathymetry points (~5 km) does not significantly increase the uncertainty of the model. A gravity uncertainty of 1 mGal introduces ~15 m of uncertainty into the modelled bathymetry (from the Bouguer slab formula, assuming a rock/water density contrast of 1.642 g cm^{-3}), so 3.2 mGal gravity uncertainty translates to ~48 m depth uncertainty. The modelled density accounts for large-scale crustal structures, but the density of the rocks at the seafloor remains uncertain. An uncertainty of 0.05 g cm^{-3} in seafloor density adds ~3% uncertainty to the relief; for example, an additional ~10 m for a typical relief of ~300 m. Linearly adding in the typical uncertainty of the bathymetry constraints themselves (an additional 10 m) gives a total uncertainty of 68 m for the bathymetry inversion.

Ocean model. We used the Regional Ocean Modeling System (version 3.6)[63] to solve the three-dimensional equations of motion with the hydrostatic and Boussinesq approximations. The equations were discretized on a 5 km horizontal grid and a 24-level terrain-following vertical coordinate system, which improved representation of processes near lower and upper boundaries. The domain was similar to that used in previous Ross Sea and Ross Ice Shelf studies[64–66] but with a new ice-shelf draft based on the Bedmap2 compilation[36] and a new sub-ice-shelf bathymetry from ROSETTA-Ice (Fig. 4a and Supplementary Fig. 4). The revised domain includes idealized representation of the unsurveyed seabed in inlets under major East Antarctic glaciers (Nimrod, Byrd, Mulock and Skelton). Bathymetry and ice-shelf draft were smoothed to satisfy numerical stability requirements related to the vertical coordinate system[67] and the minimum water column thickness used in the model was 40 m.

Surface forcing of the ocean was the same as that used in a previous model of the Ross Sea[65]. In ocean regions free of sea ice, fluxes of momentum, heat and salinity were calculated from atmospheric variables taken from the Antarctic Mesoscale Prediction System, an atmospheric forecast model[68], and climatological monthly values of cloud cover[69]. In regions covered by sea ice, surface fluxes were calculated using a coupled sea ice model[70]. Beneath the ice shelf, heat and salt fluxes were calculated as functions of the time-varying ocean temperature and

friction velocity of the uppermost model layer[65,71]. Tidal forcing was applied at open lateral boundaries[66,67]. The solution was nudged to climatological temperature and salinity depth profiles at the boundaries, and barotropic velocities at the ocean boundaries were relaxed to monthly depth-averaged circulation from a 0.25° global model[72].

We used the final state of an earlier model run[64] as the initial state of the present model runs, after interpolating model state variables to the new domain. The model was integrated for 20 additional years with a repeated annual cycle of atmospheric forcing from 15 September 2001 to 15 September 2002. The model simulation time period did not overlap the period of the ROSETTA-Ice observations, but interannual variability is not expected to play a critical role in the study performed here.

Using the temperature and salinity distribution at the end of the spin-up period, water masses (HSSW, mCDW and AASW)[24] north of the ice front were labelled with distinct passive tracers at the start of the simulation. These passive dyes then evolved according to the advection and diffusion of the model simulation. The change in distribution and concentration of these tracers demonstrates how circulation redistributes the primary water masses that ventilate the ocean cavity beneath the ice shelf (Supplementary Videos 1–3). The invasion of the ice cavity by HSSW closely follows depth-integrated transport streamlines (Fig. 4 and Supplementary Videos 1–3) near Ross Island and southward along the East Antarctic grounding line. These streamlines turn northward near the middle of the ice shelf and flow outward near Drygalski Trough. None of the streamlines, and little HSSW, crosses the tectonic boundary into the West Antarctic side of the cavity, although much of the ISW on the West Antarctic side is derived from HSSW interactions with the ice shelf on the East Antarctic side. Along Hayes Bank, near the middle of the ice shelf, mCDW enters the ice cavity and circulates no further than the south end of Roosevelt Island before turning northward. AASW is restricted to a small region, from Ross Island to Minna Bluff, where the ice shelf draft is less than about 150 m.

Supplementary Fig. 7 identifies these water masses in a characteristic hydrographic profile from near the ice front. This figure demonstrates why cold HSSW with a temperature near −1.9 °C still has the potential to melt ice because of the suppression of the in situ freezing point by high pressures under thick ice, especially near the deep grounding lines of East Antarctic outlet glaciers along the Transantarctic Mountains. The modelled melt rate in the grounding zone near Byrd Glacier is about 5 m yr^{-1}, less than the value of 12 ± 2 m yr^{-1} calculated for 1978–1979[16]. We attribute this difference to smoothing of our model grid for computational stability, which reduces the water depth at the grounding line from the measured value of ~1,800 m to ~1,400 m in the model, and unknown bathymetry around and within the inlet into which Byrd Glacier flows.

Ice shelf stratigraphy to constrain basal melt rate. Shallow Ice Radar profiles from the ROSETTA-Ice survey contain reflections that reveal the basic structure of the ice shelf and how it changes as the ice flows from the grounding line to the ice front. Stratigraphy in ice-penetrating radar profiles has previously been used to determine basal melt rates near grounding lines[73]. The ice shelf consists primarily of ice from the grounded ice sheet ('continental ice') that has crossed the grounding line, overlain by clearly layered younger ice that originated as snowfall onto the floating ice shelf. Distinct reflections at the top of the continental ice are identifiable in ROSETTA-Ice profiles across most of the ice shelf (Supplementary Fig. 8a). Several sources have been attributed to the detection of internal layers in radar profiles, such as the difference in ice fabric or dielectric contrast at an interface in the ice column[74,75]. On the Ross Ice Shelf, the ice structure is distinctly different on either side of the reflector—with clearly stratified, sub-horizontal layers above, and deformed[76] or unresolvable features below, suggesting a different mode of formation for the ice above and below. A difference in fabric is therefore the most likely explanation for the observed reflector. Further research is required to identify whether this reflector is accentuated by wind glaze, or surface crevasses near the grounding line, and whether the same processes are represented for all inputs around the ice shelf. As the continental ice flows through the ice shelf region, this interface deepens as it is buried by surface accumulation. Strain and basal melting also affect the ice shelf stratigraphy[15]. Strain will affect both the continental and ice shelf ice while basal melting affects only the continental ice, except in cases where all continental ice has been removed by basal melting.

Three sequential profiles spaced 20 km apart (Fig. 4c–e and Supplementary Fig. 8b–d) show along-flow changes in the thickness of layers above and below the strong reflector in ice originating from Byrd and Mulock glaciers. We picked the internal reflection and base of the ice shelf in the Shallow Ice Radar and Deep Ice Radar, respectively, and differenced the picks to give the thickness of the continental ice in all three lines (L830, L850 and L870). By dealing with changes in thickness of the continental ice layer, we eliminate uncertainties arising from the velocity model of the overlying firn. We estimate the accuracy of the ice thickness measurements to be of the order of 1 m. Where the internal reflector can be seen in all three lines, it is an undulating layer that undergoes deformation between L830 and L870 but maintains recognizable features. We correlated a peak in the internal layer that was visible in all three lines and measured the change in thickness (measured from the internal layer peak to the ice base) to be 39 m from L830 to L850 and 36 m from L850 to L870, giving a 75 m total change. Where the internal reflector is entirely removed, the maximum thickness of the removed layer represents a local minimum amount of basal melting. Within L830 this maximum thickness is 95 m, suggesting that our estimate of 75 m is a conservative estimate of the melting in this area.

Given the average velocity of 480 m yr^{-1} in this region (Supplementary Fig. 2b), the time interval between each radar profile is ~41 years. From the observed total thickness change of the basal unit of 75 m, the average basal thinning rate is 0.9 m yr^{-1}. Assuming steady state, the only causes of thinning of the basal unit are basal mass loss or gain, and ice flow convergence and divergence. We consider an increase in basal melt to be the most likely explanation for the observation of thinning of the lower unit of the ice shelf.

In this region, the ice shelf is undergoing compression, so strain, by itself, would thicken both the continental ice and upper layers. The average basal thinning rate of 0.9 m yr^{-1} is therefore a lower limit of the basal melting rate. Comparison with the satellite-derived melt rates from Moholdt et al.[15] was made by sampling their basal mass balance grid, given in metres per year water equivalent, in the region defined by the survey lines shown in Supplementary Fig. 2b. Basal mass balance was converted to melt rate in metres per year of ice loss using an ice density of 917 kg m^{-3}, resulting in a mean loss, by melting, of 1.2 ± 0.2 m yr^{-1}. Taking into account local thickening of ~0.33 m yr^{-1} by ice compression[15], the satellite-derived thinning rate would be ~0.9 ± 0.2 m yr^{-1}.

Data availability

The ROSETTA-Ice airborne survey data are available from http://www.ldeo.columbia.edu/polar-geophysics-group/data.

Code availability

The code used to generate ocean simulations can be accessed at https://www.myroms.org/svn/src/. Modifications to the standard code used and ancillary input data are available on request from springer@esr.org.

References

50. Clough, J. W. & Hansen, B. L. The Ross Ice Shelf Project. *Science* **203**, 433–434 (1979).
51. Konrad, H. et al. Net retreat of Antarctic glacier grounding lines. *Nat. Geosci.* **11**, 258–262 (2018).
52. Arndt, J. E. et al. The International Bathymetric Chart of the Southern Ocean (IBCSO) Version 1.0—A new bathymetric compilation covering circum-Antarctic waters. *Geophys. Res. Lett.* **40**, 3111–3117 (2013).
53. An, M. et al. S-velocity model and inferred Moho topography beneath the Antarctic Plate from Rayleigh waves. *J. Geophys. Res. Solid Earth* **120**, 359–383 (2015).
54. Shen, W. et al. The crust and upper mantle structure of Central and West Antarctica from Bayesian inversion of Rayleigh wave and receiver functions. *J. Geophys. Res. Solid Earth* **123**, 7824–7849 (2018).
55. Tinto, K. J. & Bell, R. E. Progressive unpinning of Thwaites Glacier from newly identified offshore ridge: constraints from aerogravity. *Geophys. Res. Lett.* **38**, L20503 (2011).
56. Cochran, J. R. & Bell, R. E. Inversion of icebridge gravity data for continental shelf bathymetry beneath the Larsen Ice Shelf, Antarctica. *J. Glaciol.* **58**, 540–552 (2012).
57. Muto, A. et al. Subglacial bathymetry and sediment distribution beneath Pine Island Glacier ice shelf modeled using aerogravity and in situ geophysical data: new results. *Earth Planet. Sci. Lett.* **433**, 63–75 (2016).
58. Greenbaum, J. et al. Ocean access to a cavity beneath Totten Glacier in East Antarctica. *Nat. Geosci.* **8**, 294–298 (2015).
59. Millan, R., Rignot, E., Bernier, V., Morlighem, M. & Dutrieux, P. Bathymetry of the Amundsen Sea Embayment sector of West Antarctica from Operation IceBridge gravity and other data. *Geophys. Res. Lett.* **44**, 1360–1368 (2017).
60. Boghosian, A. et al. Resolving bathymetry from airborne gravity along Greenland fjords. *J. Geophys. Res. Solid Earth* **120**, 8516–8533 (2015).
61. An, L. et al. Bed elevation of Jakobshavn Isbræ, West Greenland, from high-resolution airborne gravity and other data. *Geophys. Res. Lett.* **44**, 3728–3736 (2017).
62. Schaffer, J. et al. A global, high-resolution data set of ice sheet topography, cavity geometry, and ocean bathymetry. *Earth Syst. Sci. Data* **8**, 543–557 (2016).
63. Haidvogel, D. B. et al. Ocean forecasting in terrain-following coordinates: formulation and skill assessment of the regional ocean modeling system. *J. Comput. Phys.* **227**, 3595–3624 (2008).
64. Dinniman, M. S., Klinck, J. M. & Smith, W. O. Influence of sea ice cover and icebergs on circulation and water mass formation in a numerical circulation model of the Ross Sea, Antarctica. *J. Geophys. Res.* **112**, C11013 (2007).
65. Dinniman, M. S., Klinck, J. M. & Smith, W. O. A model study of Circumpolar Deep Water on the West Antarctic Peninsula and Ross Sea continental shelves. *Deep Sea Res. II* **58**, 1508–1523 (2011).

66. Arzeno, I. B. et al. Ocean variability contributing to basal melt rate near the ice front of Ross Ice Shelf, Antarctica. *J. Geophys. Res. Oceans* **119**, 4214–4233 (2014).
67. Mueller, R. D. et al. Impact of tide-topography interactions on basal melting of Larsen C Ice Shelf, Antarctica. *J. Geophys. Res.* **117**, C05005 (2012).
68. Bromwich, D. H., Monaghan, A. J., Manning, K. W. & Powers, J. G. Real-time forecasting for the Antarctic: an evaluation of the Antarctic Mesoscale Prediction System (AMPS). *Mon. Weather Rev.* **133**, 579–603 (2005).
69. Rossow, W. B. & Schiffer, R. A. Advances in understanding clouds from ISCCP. *Bull. Am. Meteor. Soc.* **80**, 2261–2287 (1999).
70. Budgell, W. P. Numerical simulation of ice-ocean variability in the Barents Sea region. *Ocean Dyn.* **55**, 370–387 (2005).
71. Holland, D. M. & Jenkins, A. Modeling thermodynamic ice–ocean interactions at the base of an ice shelf. *J. Phys. Oceanogr.* **29**, 1787–1800 (1999).
72. Webb, D. J, de Cuevas, B. A. & Coward, A. C. *The First Main Run of the OCCAM Global Ocean Model* (Southampton Oceanography Centre, 1998).
73. Catania, G., Hulbe, C. & Conway, H. Grounding-line basal melt rates determined using radar-derived internal stratigraphy. *J. Glaciol.* **56**, 545–554 (2010).
74. Jacobel, R. W., Scambos, T. A., Raymond, C. F. & Gades, A. M. Changes in the configuration of ice stream flow from the West Antarctic Ice Sheet. *J. Geophys. Res. Solid Earth* **101**, 5499–5504 (1996).
75. Jacobel, R. W., Gades, A. M., Gottschling, D. L., Hodge, S. M. & Wright, D. L. Interpretation of radar-detected internal layer folding in West Antarctic ice streams. *J. Glaciol.* **39**, 528–537 (1993).
76. Wright, D. L., Hodge, S. M., Bradley, J. A., Grover, T. P. & Jacobel, R. W. Instruments and methods: a digital low-frequency, surface-profiling ice-radar system. *J. Glaciol.* **36**, 112–121 (1990).